ACS APPLIED NANO MATERIALS

www.acsanm.org Article

Role of H_2 in the Substrate-Directed Synthesis of Size-tunable $MoSe_2$ Nanoribbons for Exciton Engineering

Erick C. Sadler, Tomojit Chowdhury, Reynolds Dziobek-Garrett, Chenyang Li, Ona Ambrozaite, Tim Mueller, and Thomas J. Kempa*

Cite This: *ACS Appl. Nano Mater.* 2022, 5, 11423–11428 Read Online

ACCESS | Metrics & More | Article Recommendations | Supporting Information

ABSTRACT: Recent studies of transition-metal dichalcogenide (TMD) nanoribbons have stimulated the development of synthetic strategies for the controlled growth of these dimensionally restricted crystals. We demonstrate the width-controlled synthesis of $MoSe_2$ nanoribbons grown on a designer surface comprising Si(001) treated with phosphine. Adjustment of the H_2 partial pressure in the carrier gas stream enables the nanoribbon widths to be tuned between 175 nm and almost 500 nm. Experiments and simulations suggest that H_2 exposure increases the surface coverage of hydrogen on the Si−P dimers that normally serve as favorable regions for nanoribbon nucleation and growth. Moreover, the $MoSe_2$ nanoribbons exhibit an anomalous photoluminescence blue shift whose magnitude of 60 meV is similar to that reported in optical emission spectra of MoS_2 nanoribbons. These studies demonstrate that the recently developed strategy of substrate-directed growth of nanoribbons can be extended to the selenide family of TMDs. Moreover, they expand the synthetic foundation for preparing complex TMD heterostructures, which are required for optical- and quantum-based sensors, transducers, and processors.

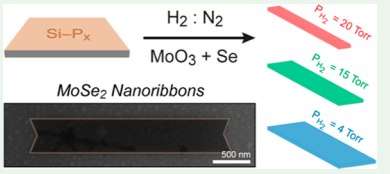

KEYWORDS: *transition-metal dichalcogenide, nanoribbon, $MoSe_2$, surface, photoluminescence, exciton*

INTRODUCTION

Transition-metal dichalcogenide (TMDs) crystals are versatile materials that evince a tunable band gap, edge-dependent electronic, magnetic, and catalytic properties, and a plethora of unique exciton and spin dynamics, especially in multi-layer assemblies.[1−8] The dimensionality, edge structure, phase, and inter-layer orientation play an important role in determining the properties of TMD crystals. While two-dimensional (2D) TMD crystals have dominated the landscape of studies over the past decade, crystals exhibiting reduced dimensionalities and more complex morphologies offer many intriguing opportunities in catalytic, electronic, optical, and quantum device studies.[9,10] With regards to 1D crystals (i.e., nanoribbons), an increased proportion, relative to 2D crystals, of edge sites to basal plane sites, lateral confinement effects, and the ability to define new interfaces and topologies render these crystals promising platforms for further research. Specifically, recent breakthroughs in the synthesis of graphene and TMD nanoribbons[11−18] have revealed that constraining the dimensionality of 2D crystals toward the 1D limit results in a tunable band gap,[19,20] enhanced thermoelectric performance,[21] ferromagnetism,[22] width-dependent phase stability,[18,23] and spatially heterogeneous electronic properties[12] (i.e., metallic edges and a semiconducting interior).

Recently, our group reported the growth of uniform and width-tunable TMD nanoribbons grown by chemical vapor deposition (CVD) over Si surfaces pre-treated with phosphine. Our unique approach complements other strategies for preparing dimensionally restricted graphene and TMD crystals, including molecular beam epitaxy,[12] ledge-directed epitaxy,[13] CVD growth through vapor−liquid−solid processes,[14,16,24,25] and highly anisotropic growth by CVD on Ge(001) and sapphire substrates.[15,26] In our work, the phosphine-treated Si(001) surfaces present a distribution of Si−P and P−P dimers that mediate heterogeneous nucleation of the MoS_2 nanoribbons. The nanoribbons are readily exfoliated from these "designer" surfaces and exhibit a width-dependent photoluminescence (PL), which is blue-shifted by up to 50 meV relative to the emission from the neutral A exciton line in 2D MoS_2.[11]

Our previous success with controlling the dimensionality of TMD nanocrystals on designer surfaces prompted the need to examine the extent to which this strategy can be applied to other TMDs. A number of considerations motivated our decision to focus on $MoSe_2$. First, the growth of $MoSe_2$ and other selenides in the TMD family requires H_2 gas to promote reduction, and these materials exhibit accelerated growth times compared to MoS_2.[27−31] The role of H_2 during substrate-guided growth of $MoSe_2$ nanoribbons must be addressed to understand how we must adapt our strategy to accommodate new material systems. Second, the preparation of nanoribbons

Received: June 6, 2022
Accepted: June 28, 2022
Published: July 25, 2022

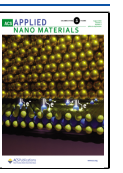

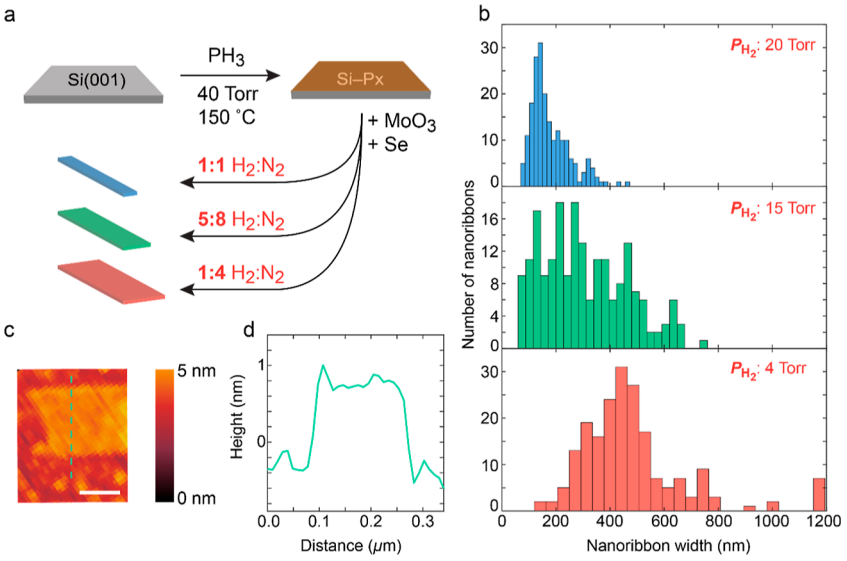

Figure 1. Control of the $MoSe_2$ nanoribbon width through H_2 partial pressure. (a) Schematic illustrating the gas-phase functionalization of Si(001) with PH_3 to yield the Si−P_x surface. Following this, metal oxide and chalcogen powders are heated in the presence of H_2 and N_2 in varying relative concentrations. Growth under these conditions on the Si−P_x surface furnishes nanoribbons of tunable width. (b) Histograms of nanoribbon width generated from syntheses carried out at H_2 partial pressures of 20, 15, and 4 Torr. Data were sampled using 25 equally sized bins. 2D crystals and crystals not conforming to a nanoribbon morphology (see the Methods section) were not counted in these histograms. (c) Atomic force micrograph of a $MoSe_2$ nanoribbon. Scale bar: 100 nm. (d) Height profile of a $MoSe_2$ nanoribbon measured along the green-dotted line in (c).

encompassing a broad class of TMDs will enable the assembly of complex axial and layered superlattices that could serve as promising platforms for excitonic, electronic, and quantum information studies.

Herein, we examine factors dictating the controlled synthesis of $MoSe_2$ nanoribbons on a phosphine (PH_3)-treated Si designer surface. To prepare the designer growth substrates, we treat hydrogen-terminated Si(001) surfaces with PH_3 gas at 150 °C in a CVD reactor. $MoSe_2$ nanoribbons are grown on this substrate in the same CVD reactor at 700 °C at several different H_2 partial pressures. We identify that the nanoribbon width is a sensitive function of the H_2 partial pressure in the carrier gas mixture and propose that modulation of the designer surface composition is responsible.

RESULTS AND DISCUSSION

After functionalizing H-terminated Si(001) surfaces with PH_3 to form the "Si−P_x" crystal growth surface, we grew $MoSe_2$ crystals from MoO_3 and Se under several different carrier gas regimens (Figure 1). Based on previously reported cluster expansion calculations, the Si−P_x surface prepared here (at 150 °C and P_{PH_3} = 8 Torr) likely comprises Si−P and P_2 dimers. $MoSe_2$ crystals were grown over this Si−P_x surface in the presence of three distinct carrier gas streams, each comprising a mixture of H_2 and N_2 in the following H_2/N_2 ratios: 1:1, 1:1.6, and 1:4 (Figure 1a). Under the CVD reactor conditions employed here, the H_2 partial pressures for these three conditions are calculated to be 20, 15, and 4 Torr, respectively. Scanning electron microscopy (SEM) images of samples prepared under these conditions reveal nanoribbon crystals produced at significant yields (Figure S1).

Additional SEM images of the $MoSe_2$ nanoribbons were collected and analyzed to generate histograms of width for nanoribbons prepared at each of the three carrier gas conditions (Figures S2, S3, and 2a). Notably, the average nanoribbon width increases from 175 to 485 nm as the partial

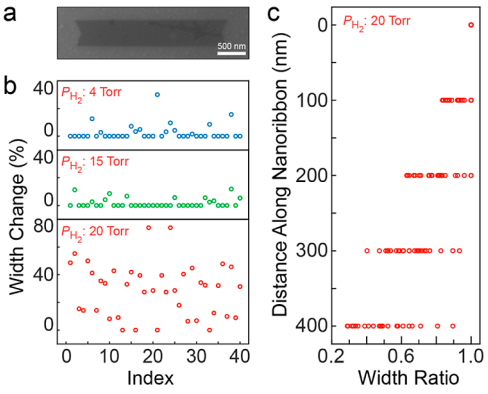

Figure 2. Nanoribbon width uniformity as a function of H_2 partial pressure. (a) SEM image of a single $MoSe_2$ nanoribbon grown at a H_2 partial pressure of 15 Torr. Scale bar: 500 nm. (b) Scatter plots of the change in width along individual $MoSe_2$ nanoribbons. Each data point corresponds to the percent change between the nanoribbon width measured at the midpoint and at a point 350 nm along its length. Forty nanoribbons were sampled for each of the three H_2 partial pressures and widths were measured edge-to-edge. (c) Scatter plot of the change in width of nanoribbons grown at P_{H_2} = 20 Torr as a function of their length starting at the midpoint. Widths were measured every 100 up to 400 nm away from the nanoribbon midpoint. These data provide an aggregate view of the gradual and consistent tapering of $MoSe_2$ nanoribbons grown at the highest H_2 partial pressure. 2D crystals and crystals not conforming to a nanoribbon morphology (see the Methods section) were not considered in the assays shown in "b" and "c".

pressure of H_2 in the carrier gas mixture decreases from 20 to 4 Torr (Figure 1b). The reaction performed at the lowest H_2 partial pressure (4 Torr) not only yields the widest and shortest nanoribbons but also gives rise to the highest fraction of multiply nucleated $MoSe_2$ crystals (Figure S2). This finding is reflected in the lowest H_2 partial pressure condition (4 Torr), yielding nanoribbons with the lowest average aspect

https://doi.org/10.1021/acsanm.2c02477
ACS Appl. Nano Mater. 2022, 5, 11423−11428

ratio (Figure S4). Our current findings regarding the morphology of $MoSe_2$ nanoribbons grown at the lowest H_2 partial pressure are consistent with our previous observations,[11] which showed that higher PH_3 partial pressures during the Si surface functionalization step also yield wider and more extensively nucleated TMD nanoribbons. The morphology of the nanoribbons was further characterized by atomic force microscopy (AFM), which revealed a nanoribbon height of ~1 nm, which is in accordance with monolayer-thick $MoSe_2$ (Figure 1c,d). Finally, we confirmed that PH_3-functionalized Si(111) surfaces do not support nanoribbon growth, thereby confirming the unique role of the Si−P_x surface, which is derived from Si(001), in spawning nanoribbon growth (Figure S5). Together, these data show not only that $MoSe_2$ nanoribbons can be readily prepared on Si−P_x surfaces but also that bottom-up control of their width is possible through careful adjustment of the H_2 partial pressure during the TMD growth phase.

During our surveys of $MoSe_2$ nanoribbons grown under the three conditions discussed above, we identified deviations, to varying degrees, in their width along their longitudinal axis. An analysis reveals that nanoribbons prepared at H_2 partial pressures of 15 and 4 Torr exhibit an average maximum change in their width of 1.7 and 2.6%, respectively (Figure 2a,b). This high intra-ribbon width uniformity contrasts with what is a significant change in intra-ribbon width for $MoSe_2$ nanoribbons grown at a H_2 partial pressure of 20 Torr. Focusing on nanoribbons grown at this highest H_2 condition, we identify several features. First, the nanoribbons gradually taper at their ends to approximately 50% of their full width on average (Figure 2c). Second, this pronounced taper often produces $MoSe_2$ nanoribbons with widths below 100 nm (Figure S6). This latter result suggests that tuning of the carrier gas pressure and type, in conjunction with our previous result[11] demonstrating width control through manipulating the Si−P_x surface, may be sufficient to realize the controlled growth of ultra-narrow (e.g., <10 nm wide) nanoribbons with unique morphologies, edges, and dimensions. Subject to quantum confinement effects due to their dramatically reduced dimensionality, ultra-narrow nanoribbons are compelling platforms on which to study single photon emission and charge density wave phenomena.[32−34]

The foregoing data show that low H_2 partial pressures favor $MoSe_2$ nanoribbons that are wide and have a greater propensity for multi-site nucleation, while high H_2 partial pressures favor narrow and tapered nanoribbons. We hypothesize that H_2 alters the composition of the Si−P_x surface as it is introduced during the $MoSe_2$ growth step and thereby influences the extent of nanoribbon nucleation.

To understand how $MoSe_2$ nanoribbon morphology is linked to the composition of the Si−P_x surface, we first performed cluster expansions[35,36] to gain insight into the equilibrium composition and configuration of this surface. Simulations reveal that the equilibrium fractional P atom coverage over the Si(001) surface varies as a function of the partial pressure of PH_3 applied during the treatment step (Figure 3). Several features are revealed by these data. First, while P atoms are predicted to comprise up to 54% of the surface for a PH_3 partial pressure of 8 Torr, there is a notably wide range of PH_3 partial pressures (0.08−4.5 Torr) over which the P atom concentration is "saturated" at a steady level of ~50% of surface sites. Second, a Monte Carlo[37] snapshot of the equilibrium surface taken for a PH_3 partial pressure (0.02 Torr) just below the aforementioned saturation region shows that nearly half of the Si surface sites are occupied with P in the form of Si−P dimers. Third, a Monte Carlo snapshot of the equilibrium surface taken for a PH_3 partial pressure (8 Torr) just above the aforementioned saturation region reveals a surface predominantly covered by Si−P with the appearance of some P_2 dimers. Taking into consideration the above calculations and the fact that our Si surface treatment reaction is performed at a PH_3 partial pressure of 8 Torr, we predict that the phosphorus on our Si−P_x surface is present predominantly in the form of Si−P dimers.

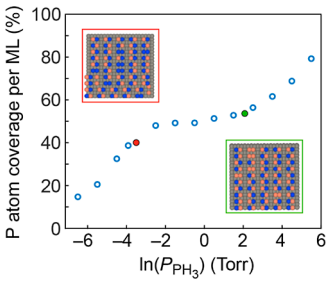

Figure 3. Numerical simulations of the Si−P_x surface. The % P atom coverage in the surface monolayer as a function of PH_3 partial pressure as obtained through cluster expansion calculations. Salmon and blue spheres represent P and Si atoms, respectively. Insets: Monte Carlo simulation images for P atom coverage at the points indicated in red and green in the scatter plot. The red and green boxed simulation images are at PH_3 partial pressures of 0.02 and 8 Torr, respectively. The simulation temperature was 150 °C.

Once the Si−P_x surface is exposed to higher temperatures (700 °C) and H_2 during the $MoSe_2$ crystal growth step, it is expected that the surface will change. Our calculations predict that at this temperature and a H_2 partial pressure of approximately 1 Torr, roughly half of the silicon atoms in Si−P dimers on a model Si−P surface will become terminated by hydrogen. At approximately 30 Torr, nearly all silicon atoms in Si−P dimers are predicted to become H-terminated (Table S1). These results suggest that in our experiments, there is a significant increase in hydrogen surface coverage on Si−P dimers as the hydrogen partial pressure increases from 4 to 20 Torr. We note a slight reduction in surface roughness upon PH_3 functionalization and then a slight increase in roughness at $MoSe_2$ growth temperatures, which is consistent with the stripping of P-containing moieties from the Si−P_x surface (Figure S7). We hypothesize that increasing hydrogen coverage on regions of the surface most favorable for $MoSe_2$ crystal formation (i.e., Si−P domains) restricts the nucleation and growth of these crystals, resulting in narrower ribbons. We have previously observed that lower partial pressures of PH_3 introduced during the surface treatment step resulted in the growth of narrower nanoribbons.[11] Finally, we note that an increased incidence of V-shaped or Y-shaped $MoSe_2$ crystals at lower H_2 partial pressures (i.e., 4 Torr) is consistent with the aforementioned multi-site nucleation (Figure S2), which is more likely when the effective Si−P domain size is increased due to reduced action of H_2. Taken together, these observations suggest that the influence of phosphorous on the surface is at least partially mediated by hydrogen adsorbed on nearby silicon atoms.

Having established the role of H_2 in the width-controlled growth of $MoSe_2$ nanoribbons, we assessed their photoemission properties. For these studies, we collected far-field

https://doi.org/10.1021/acsanm.2c02477
ACS Appl. Nano Mater. 2022, 5, 11423−11428

Raman and PL spectra from samples, both on an Si−P_x surface, of 2D $MoSe_2$ crystals and of $MoSe_2$ nanoribbons with an average width of ∼400 nm. Raman spectra of the 2D $MoSe_2$ crystals and the $MoSe_2$ nanoribbons identify a peak at 240 cm^{-1} (Figure 4a). Based on previous studies, this peak can be

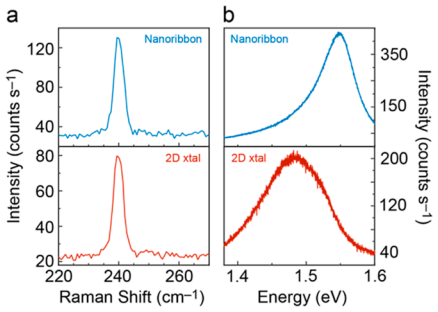

Figure 4. Optical properties of $MoSe_2$ nanoribbons compared to 2D $MoSe_2$ crystals. (a) Raman spectra of a nanoribbon (top, blue) and 2D (bottom, red) $MoSe_2$ crystals. (b) PL spectra of a nanoribbon (top, blue) and 2D (bottom, red) $MoSe_2$ crystals. Both the nanoribbon and 2D crystals were measured on an Si−P_x surface.

assigned to the A_{1g} mode of monolayer $MoSe_2$.[30,38−41] PL spectra of the two samples reveal that the nanoribbon emission peak at 1.54 eV is blue-shifted relative to the emission peak of 2D $MoSe_2$ at 1.48 eV, where the latter is consistent with emission from the neutral exciton of $MoSe_2$ (Figure 4b).[40−43] The 60 meV blue-shifted PL exhibited by the $MoSe_2$ nanoribbons here is consistent with the 50 meV blue-shifted PL reported for MoS_2 nanoribbons (relative to 2D MoS_2) and may likewise be ascribed to their reduced dimensionality.[11] Additional PL measurements taken from different crystals at a different substrate location evince similar shifts in emission profiles between $MoSe_2$ nanoribbons and 2D flakes (Figure S8). While the $MoSe_2$ nanoribbons may proceed through similar pathways of optical emission as previously reported in MoS_2 nanoribbons, the exact origin of the consistently blue-shifted PL in dimensionally restricted TMDs is under investigation.

■ CONCLUSIONS

We demonstrate the controlled synthesis of $MoSe_2$ nanoribbons on a phosphine-treated designer surface. We also show that the nanoribbon widths can be tuned between 175 and almost 500 nm through the adjustment of the H_2 partial pressure in the carrier gas stream. We propose that hydrogen adsorbs on Si−P dimers that serve as preferential nucleation sites for nanoribbon growth, thereby tuning the crystal width. Finally, we show that the nanoribbons exhibit an anomalous PL blue shift of a similar magnitude to that observed in previously reported MoS_2 nanoribbons. This work not only expands the concept of substrate-directed growth of nanoribbons to the selenide family of TMDs but also lays the foundation for preparation of complex low-dimensional TMD heterostructures of relevance to quantum information studies and all-optical information processing.

■ METHODS

Synthesis of $MoSe_2$ Nanoribbons. We utilize a gas phase synthesis method, which has been described in our previous work.[11] In this method, H-terminated Si(001) surfaces, prepared by fully etching SiO_2 on Si(001) substrates in hydrogen fluoride, are treated with phosphine gas (Air Liquide, 20% PH_3 in He) at a total reactor pressure of 40 Torr (P_{PH_3} = 8 Torr) and temperature of 150 °C. The CVD reactor was heated to 150 °C at a rate of 12.5 °C/min and then allowed to remain at 150 °C for 60 min. The PH_3 flow was set to 10 sccm and the reactor pressure held at 40 Torr for the duration of the heating ramp and hold time. After 60 min, the surface treatment reaction was stopped by shutting off the flow of PH_3 gas and introducing N_2 to cool the reactor to 100 °C. At 100 °C, the treated substrate was removed and placed face down on a ceramic boat containing 10 mg of MoO_3 powder. This boat and substrate were then placed in the central zone (of three total isolable heating zones) of the CVD reactor tube. Approximately 140 mg of Se powder was loaded in a separate ceramic boat, and this boat was then placed in the upstream zone of the CVD reactor. Once loaded, the system was evacuated to a base pressure of 1 × 10^{-5} Torr. The system was then pressurized to 40 Torr with a gas stream consisting of an 8 sccm flow rate of N_2 and varying flow rates of H_2 gas to realize the partial pressures noted in the paper. Once the reactor reached a pressure of 40 Torr, the CVD reactor tube was heated up to 550−700 °C over the course of 8 min. This reactor was held at this temperature for 10 min and thereafter allowed to cool to 500 °C while maintaining the gas flows and pressure. After reaching a temperature of 500 °C, the reactor was evacuated to the base pressure and then cooled under a 200 sccm stream of N_2.

Raman and PL Spectroscopy. Raman and PL spectra were measured in a confocal microscope system equipped with a HORIBA Jobin Yvon T46000 spectrometer and a liquid N_2-cooled charge-coupled device detector. Crystals were excited with an Ar^+/Kr^+ laser at 514 nm. This laser output was focused through a 100× objective (Olympus) to a ∼1 μm spot size. The laser power was 1 mW.

Scanning Electron Microscopy. High-resolution SEM images were obtained using a Tescan Mira3 GMU scanning electron microscope at an acceleration voltage of 5 or 10 kV. MATLAB (R2020) was used to extract quantitative values of the yield, dimensions, and aspect ratio of nanoribbons from SEM images. Crystals were classified as nanoribbons if they fulfilled the following criteria: (1) the crystal exhibits a single longitudinal axis (i.e., no "V"- or "Y"-shaped crystals arising from the growth from more than one facet of the nucleosome) and (2) the crystal exhibits no significant deviations from its width (i.e., no branches, triangular outgrowths, etc.). The one exception to criterion 2 is that monotonically tapered nanoribbons were included as these morphologies were the dominant class at P_{H_2} = 20 Torr.

Atomic Force Microscopy. AFM images were taken using an Asylum MFP-3D in tapping mode with silicon tips. Scans were taken with a resolution of 512 × 512 pixels and a scan speed of less than 0.5 Hz. Scan images were then processed in Gwyddion with a masking of outliers and polynomial background subtraction. Line-scans to assess nanoribbon heights were then taken across the width of a nanoribbon with averaging over four adjacent scans.[48]

Computational Methods. To predict the equilibrium structures of the Si−P_x surfaces, we created a cluster expansion[35] trained by density functional theory (DFT)[45] calculations and then performed grand canonical Monte Carlo[37] simulations. In the cluster expansion, we assume that each site can be occupied by either a Si atom, a P atom, or a vacancy (only in the outmost layer) based on the (1 × 2) dimer-reconstructed Si(001) surface.[44] We fit the cluster expansion using the Bayesian method.[36] DFT calculations were performed using the Vienna Ab initio Simulation Package[46] with the revised Perdew−Burke−Ernzerhof[47] exchange-correlation functional. The Brillouin zone was sampled using generalized Monkhorst−Pack grids generated by the *k*-point grid server[49] with a minimum distance of 20 Å between real-space lattice points. Monte Carlo simulations[37] were run from a high temperature (1300 °C) and then decreased in steps by a factor of $4^{0.05}$ until reaching the experimental temperature of 150 °C. The number of Monte Carlo iterations, at each temperature, was 1,440,000 in a 24 × 12 supercell. We used the same computational methods as in our previous work,[11] in which additional details are provided.

https://doi.org/10.1021/acsanm.2c02477
ACS Appl. Nano Mater. 2022, 5, 11423−11428

■ ASSOCIATED CONTENT

Supporting Information

The Supporting Information is available free of charge at https://pubs.acs.org/doi/10.1021/acsanm.2c02477.

SEM images of nanoribbons prepared at various H_2 partial pressures, measured crystal dimensions, AFM maps of the growth substrate, additional Raman and PL data, and calculations of the H adsorption and coverage on Si−Si and Si−P dimers (PDF)

■ AUTHOR INFORMATION

Corresponding Author

Thomas J. Kempa − *Department of Chemistry, Johns Hopkins University, Baltimore, Maryland 21218, United States; Department of Materials Science & Engineering, Johns Hopkins University, Baltimore, Maryland 21218, United States;* orcid.org/0000-0002-1672-8325; Email: tkempa@jhu.edu

Authors

Erick C. Sadler − *Department of Chemistry, Johns Hopkins University, Baltimore, Maryland 21218, United States*

Tomojit Chowdhury − *Department of Chemistry, Johns Hopkins University, Baltimore, Maryland 21218, United States;* Present Address: Department of Chemistry, University of Chicago, Chicago, Illinois 60637, United States; orcid.org/0000-0002-6841-0642

Reynolds Dziobek-Garrett − *Department of Chemistry, Johns Hopkins University, Baltimore, Maryland 21218, United States*

Chenyang Li − *Department of Materials Science & Engineering, Johns Hopkins University, Baltimore, Maryland 21218, United States;* orcid.org/0000-0002-5155-4631

Ona Ambrozaite − *Department of Chemistry, Johns Hopkins University, Baltimore, Maryland 21218, United States*

Tim Mueller − *Department of Materials Science & Engineering, Johns Hopkins University, Baltimore, Maryland 21218, United States;* orcid.org/0000-0001-8284-7747

Complete contact information is available at: https://pubs.acs.org/10.1021/acsanm.2c02477

Author Contributions

E.C.S. and T.J.K. conceived and designed the study. E.C.S. performed the syntheses and carried out characterization with assistance from T.C., R.D.-G., O. A., and T.J.K. Computational work was designed by T.M. and carried out by C.L. with assistance from T.M. All authors contributed to the analysis of results. E.C.S. and T.J.K. wrote the manuscript with input from all co-authors.

Funding

T.J.K. acknowledges funding for this study by the Young Faculty Award program of the Defense Advanced Research Projects Agency (DARPA) and by the Army Research Office under the grant W911NF-21-1-0351. The views, opinions, and/or findings expressed are those of the authors and should not be interpreted as representing the official views or policies of the Department of Defense or the U.S. Government. T.J.K. also acknowledges funding from a National Science Foundation (DMR-1848046) CAREER grant which supported characterization studies in this work. T.C. acknowledges support through an Ernest M. Marks Award from Johns Hopkins University.

Notes

The authors declare no competing financial interest.

■ REFERENCES

(1) Seyler, K. L.; Rivera, P.; Yu, H.; Wilson, N. P.; Ray, E. L.; Mandrus, D. G.; Yan, J.; Yao, W.; Xu, X. Signatures of Moiré-Trapped Valley Excitons in $MoSe_2/WSe_2$ Heterobilayers. *Nature* **2019**, *567*, 66−70.

(2) Tran, K.; Moody, G.; Wu, F.; Lu, X.; Choi, J.; Kim, K.; Rai, A.; Sanchez, D. A.; Quan, J.; Singh, A.; Embley, J.; Zepeda, A.; Campbell, M.; Autry, T.; Taniguchi, T.; Watanabe, K.; Lu, N.; Banerjee, S. K.; Silverman, K. L.; Kim, S.; Tutuc, E.; Yang, L.; MacDonald, A. H.; Li, X. Evidence for Moiré Excitons in van Der Waals Heterostructures. *Nature* **2019**, *567*, 71−75.

(3) Zhang, Y.; Chang, T.-R.; Zhou, B.; Cui, Y.-T.; Yan, H.; Liu, Z.; Schmitt, F.; Lee, J.; Moore, R.; Chen, Y.; Lin, H.; Jeng, H.-T.; Mo, S.-K.; Hussain, Z.; Bansil, A.; Shen, Z.-X. Direct Observation of the Transition from Indirect to Direct Bandgap in Atomically Thin Epitaxial $MoSe_2$. *Nat. Nanotechnol.* **2014**, *9*, 111−115.

(4) Mak, K. F.; Lee, C.; Hone, J.; Shan, J.; Heinz, T. F. Atomically Thin MoS_2: A New Direct-Gap Semiconductor. *Phys. Rev. Lett.* **2010**, *105*, 136805.

(5) Mak, K. F.; Shan, J. Photonics and Optoelectronics of 2D Semiconductor Transition Metal Dichalcogenides. *Nat. Photonics* **2016**, *10*, 216−226.

(6) Voiry, D.; Yang, J.; Chhowalla, M. Recent Strategies for Improving the Catalytic Activity of 2D TMD Nanosheets Toward the Hydrogen Evolution Reaction. *Adv. Mater.* **2016**, *28*, 6197−6206.

(7) Choudhuri, I.; Bhauriyal, P.; Pathak, B. Recent Advances in Graphene-like 2D Materials for Spintronics Applications. *Chem. Mater.* **2019**, *31*, 8260−8285.

(8) Huang, Y. L.; Chen, Y.; Zhang, W.; Quek, S. Y.; Chen, C.-H.; Li, L.-J.; Hsu, W.-T.; Chang, W.-H.; Zheng, Y. J.; Chen, W.; Wee, A. T. S. Bandgap Tunability at Single-Layer Molybdenum Disulphide Grain Boundaries. *Nat. Commun.* **2015**, *6*, 6298.

(9) Chowdhury, T.; Sadler, E. C.; Kempa, T. J. Progress and Prospects in Transition-Metal Dichalcogenide Research Beyond 2D. *Chem. Rev.* **2020**, *120*, 12563−12591.

(10) Yagmurcukardes, M.; Peeters, F. M.; Senger, R. T.; Sahin, H. Nanoribbons: From Fundamentals to State-of-the-Art Applications. *Appl. Phys. Rev.* **2016**, *3*, 041302.

(11) Chowdhury, T.; Kim, J.; Sadler, E. C.; Li, C.; Lee, S. W.; Jo, K.; Xu, W.; Gracias, D. H.; Drichko, N. V.; Jariwala, D.; Brintlinger, T. H.; Mueller, T.; Park, H.-G.; Kempa, T. J. Substrate-Directed Synthesis of MoS_2 Nanocrystals with Tunable Dimensionality and Optical Properties. *Nat. Nanotechnol.* **2020**, *15*, 29−34.

(12) Cheng, F.; Xu, H.; Xu, W.; Zhou, P.; Martin, J.; Loh, K. P. Controlled Growth of 1D $MoSe_2$ Nanoribbons with Spatially Modulated Edge States. *Nano Lett.* **2017**, *17*, 1116−1120.

(13) Aljarb, A.; Fu, J.-H.; Hsu, C.-C.; Chuu, C.-P.; Wan, Y.; Hakami, M.; Naphade, D. R.; Yengel, E.; Lee, C.-J.; Brems, S.; Chen, T.-A.; Li, M.-Y.; Bae, S.-H.; Hsu, W.-T.; Cao, Z.; Albaridy, R.; Lopatin, S.; Chang, W.-H.; Anthopoulos, T. D.; Kim, J.; Li, L.-J.; Tung, V. Ledge-Directed Epitaxy of Continuously Self-Aligned Single-Crystalline Nanoribbons of Transition Metal Dichalcogenides. *Nat. Mater.* **2020**, *19*, 1300−1306.

(14) Sutter, P.; Wimer, S.; Sutter, E. Chiral Twisted van Der Waals Nanowires. *Nature* **2019**, *570*, 354−357.

(15) Way, A. J.; Jacobberger, R. M.; Arnold, M. S. Seed-Initiated Anisotropic Growth of Unidirectional Armchair Graphene Nanoribbon Arrays on Germanium. *Nano Lett.* **2018**, *18*, 898−906.

(16) Li, S.; Lin, Y.-C.; Zhao, W.; Wu, J.; Wang, Z.; Hu, Z.; Shen, Y.; Tang, D.-M.; Wang, J.; Zhang, Q.; Zhu, H.; Chu, L.; Zhao, W.; Liu, C.; Sun, Z.; Taniguchi, T.; Osada, M.; Chen, W.; Xu, Q.-H.; Wee, A. T. S.; Suenaga, K.; Ding, F.; Eda, G. Vapour−Liquid−Solid Growth of Monolayer MoS_2 Nanoribbons. *Nat. Mater.* **2018**, *17*, 535−542.

(17) Chen, Y.; Cui, P.; Ren, X.; Zhang, C.; Jin, C.; Zhang, Z.; Shih, C. K. Fabrication of $MoSe_2$ Nanoribbons via an Unusual Morphological Phase Transition. *Nat. Commun.* **2017**, *8*, 15135.

(18) Huang, W.; Wang, X.; Ji, X.; Zhang, Z.; Jin, C. In-Situ Fabrication of Mo_6S_6-Nanowire-Terminated Edges in Monolayer Molybdenum Disulfide. *Nano Res.* **2018**, *11*, 5849−5857.
(19) Han, M. Y.; Özyilmaz, B.; Zhang, Y.; Kim, P. Energy Band-Gap Engineering of Graphene Nanoribbons. *Phys. Rev. Lett.* **2007**, *98*, 206805.
(20) Dolui, K.; Pemmaraju, C. D.; Sanvito, S. Electric Field Effects on Armchair MoS_2 Nanoribbons. *ACS Nano* **2012**, *6*, 4823−4834.
(21) Zhang, Z.; Xie, Y.; Peng, Q.; Chen, Y. A Theoretical Prediction of Super High-Performance Thermoelectric Materials Based on MoS_2/WS_2 Hybrid Nanoribbons. *Sci. Rep.* **2016**, *6*, 21639.
(22) Botello-Méndez, A. R.; López-Urías, F.; Terrones, M.; Terrones, H. Metallic and Ferromagnetic Edges in Molybdenum Disulfide Nanoribbons. *Nanotechnology* **2009**, *20*, 325703.
(23) Zan, W.; Zhang, Z.; Yang, Y.; Yao, X.; Li, S.; Yakobson, B. I. Width-Dependent Phase Crossover in Transition Metal Dichalcogenide Nanoribbons. *Nanotechnology* **2018**, *30*, 075701.
(24) Duan, Z.; Chen, T.; Shi, J.; Li, J.; Song, K.; Zhang, C.; Ding, S.; Li, B.; Wang, G.; Hu, S.; He, X.; He, C.; Xu, H.; Liu, X.; Jin, C.; Zhong, J.; Hao, G. Space-Confined and Substrate-Directed Synthesis of Transition-Metal Dichalcogenide Nanostructures with Tunable Dimensionality. *Sci. Bull.* **2020**, *65*, 1013−1021.
(25) Chen, T.; Hao, G.; Wang, G.; Li, B.; Kou, L.; Yang, H.; Zheng, X.; Zhong, J. Controlled Growth of Atomically Thin $MoSe_2$ Films and Nanoribbons by Chemical Vapor Deposition. *2D Mater.* **2019**, *6*, 025002.
(26) Ma, Z.; Wang, S.; Deng, Q.; Hou, Z.; Zhou, X.; Li, X.; Cui, F.; Si, H.; Zhai, T.; Xu, H. Epitaxial Growth of Rectangle Shape MoS_2 with Highly Aligned Orientation on Twofold Symmetry A-Plane Sapphire. *Small* **2020**, *16*, 2000596.
(27) Chang, Y.-H.; Zhang, W.; Zhu, Y.; Han, Y.; Pu, J.; Chang, J.-K.; Hsu, W.-T.; Huang, J.-K.; Hsu, C.-L.; Chiu, M.-H.; Takenobu, T.; Li, H.; Wu, C.-I.; Chang, W.-H.; Wee, A. T. S.; Li, L.-J. Monolayer $MoSe_2$ Grown by Chemical Vapor Deposition for Fast Photodetection. *ACS Nano* **2014**, *8*, 8582−8590.
(28) Kong, D.; Wang, H.; Cha, J. J.; Pasta, M.; Koski, K. J.; Yao, J.; Cui, Y. Synthesis of MoS_2 and $MoSe_2$ Films with Vertically Aligned Layers. *Nano Lett.* **2013**, *13*, 1341−1347.
(29) Lu, X.; Utama, M. I. B.; Lin, J.; Gong, X.; Zhang, J.; Zhao, Y.; Pantelides, S. T.; Wang, J.; Dong, Z.; Liu, Z.; Zhou, W.; Xiong, Q. Large-Area Synthesis of Monolayer and Few-Layer $MoSe_2$ Films on SiO_2 Substrates. *Nano Lett.* **2014**, *14*, 2419−2425.
(30) Wang, X.; Gong, Y.; Shi, G.; Chow, W. L.; Keyshar, K.; Ye, G.; Vajtai, R.; Lou, J.; Liu, Z.; Ringe, E.; Tay, B. K.; Ajayan, P. M. Chemical Vapor Deposition Growth of Crystalline Monolayer $MoSe_2$. *ACS Nano* **2014**, *8*, 5125−5131.
(31) Xia, J.; Huang, X.; Liu, L.-Z.; Wang, M.; Wang, L.; Huang, B.; Zhu, D.-D.; Li, J.-J.; Gu, C.-Z.; Meng, X.-M. CVD Synthesis of Large-Area, Highly Crystalline $MoSe_2$ Atomic Layers on Diverse Substrates and Application to Photodetectors. *Nanoscale* **2014**, *6*, 8949−8955.
(32) Koperski, M.; Nogajewski, K.; Arora, A.; Cherkez, V.; Mallet, P.; Veuillen, J.-Y.; Marcus, J.; Kossacki, P.; Potemski, M. Single Photon Emitters in Exfoliated WSe_2 Structures. *Nat. Nanotechnol.* **2015**, *10*, 503−506.
(33) He, Y.-M.; Clark, G.; Schaibley, J. R.; He, Y.; Chen, M.-C.; Wei, Y.-J.; Ding, X.; Zhang, Q.; Yao, W.; Xu, X.; Lu, C.-Y.; Pan, J.-W. Single Quantum Emitters in Monolayer Semiconductors. *Nat. Nanotechnol.* **2015**, *10*, 497−502.
(34) Hor, Y. S.; Xiao, Z. L.; Welp, U.; Ito, Y.; Mitchell, J. F.; Cook, R. E.; Kwok, W. K.; Crabtree, G. W. Nanowires and Nanoribbons of Charge-Density-Wave Conductor $NbSe_3$. *Nano Lett.* **2005**, *5*, 397−401.
(35) Sanchez, J. M.; Ducastelle, F.; Gratias, D. Generalized Cluster Description of Multicomponent Systems. *Phys. A* **1984**, *128*, 334−350.
(36) Mueller, T.; Ceder, G. Bayesian Approach to Cluster Expansions. *Phys. Rev. B: Condens. Matter Mater. Phys.* **2009**, *80*, 024103.
(37) Metropolis, N.; Rosenbluth, A. W.; Rosenbluth, M. N.; Teller, A. H.; Teller, E. Equation of State Calculations by Fast Computing Machines. *J. Chem. Phys.* **1953**, *21*, 1087−1092.
(38) Chen, S.-Y.; Zheng, C.; Fuhrer, M. S.; Yan, J. Helicity-Resolved Raman Scattering of MoS_2 , $MoSe_2$, WS_2 , and WSe_2 Atomic Layers. *Nano Lett.* **2015**, *15*, 2526−2532.
(39) Nam, D.; Lee, J.-U.; Cheong, H. Excitation Energy Dependent Raman Spectrum of $MoSe_2$. *Sci. Rep.* **2015**, *5*, 17113.
(40) Tonndorf, P.; Schmidt, R.; Böttger, P.; Zhang, X.; Börner, J.; Liebig, A.; Albrecht, M.; Kloc, C.; Gordan, O.; Zahn, D. R. T.; Michaelis de Vasconcellos, S.; Bratschitsch, R. Photoluminescence Emission and Raman Response of Monolayer MoS2, MoSe2, and WSe2. *Opt. Express* **2013**, *21*, 4908−4916.
(41) Chow, P. K.; Jacobs-Gedrim, R. B.; Gao, J.; Lu, T.-M.; Yu, B.; Terrones, H.; Koratkar, N. Defect-Induced Photoluminescence in Monolayer Semiconducting Transition Metal Dichalcogenides. *ACS Nano* **2015**, *9*, 1520−1527.
(42) Han, H.-V.; Lu, A.-Y.; Lu, L.-S.; Huang, J.-K.; Li, H.; Hsu, C.-L.; Lin, Y.-C.; Chiu, M.-H.; Suenaga, K.; Chu, C.-W.; Kuo, H.-C.; Chang, W.-H.; Li, L.-J.; Shi, Y. Photoluminescence Enhancement and Structure Repairing of Monolayer $MoSe_2$ by Hydrohalic Acid Treatment. *ACS Nano* **2016**, *10*, 1454−1461.
(43) Wang, G.; Palleau, E.; Amand, T.; Tongay, S.; Marie, X.; Urbaszek, B. Polarization and Time-Resolved Photoluminescence Spectroscopy of Excitons in $MoSe_2$ Monolayers. *Appl. Phys. Lett.* **2015**, *106*, 112101.
(44) Wang, Y.; Chen, X.; Hamers, R. J. Atomic-Resolution Study of Overlayer Formation and Interfacial Mixing in the Interaction of Phosphorus with Si(001). *Phys. Rev. B: Condens. Matter Mater. Phys.* **1994**, *50*, 4534−4547.
(45) Kohn, W.; Sham, L. J. Self-Consistent Equations Including Exchange and Correlation Effects. *Phys. Rev.* **1965**, *140*, A1133−A1138.
(46) Kresse, G.; Hafner, J. Ab Initio Molecular Dynamics for Liquid Metals. *Phys. Rev. B: Condens. Matter Mater. Phys.* **1993**, *47*, 558−561.
(47) Hammer, B.; Hansen, L. B.; Nørskov, J. K. Improved Adsorption Energetics within Density-Functional Theory Using Revised Perdew-Burke-Ernzerhof Functionals. *Phys. Rev. B: Condens. Matter Mater. Phys.* **1999**, *59*, 7413−7421.
(48) Blöchl, P. E. Projector Augmented-Wave Method. *Phys. Rev. B: Condens. Matter Mater. Phys.* **1994**, *50*, 17953−17979.
(49) Wisesa, P.; McGill, K. A.; Mueller, T. Efficient Generation of Generalized Monkhorst-Pack Grids through the Use of Informatics. *Phys. Rev. B* **2016**, *93*, 155109.

https://doi.org/10.1021/acsanm.2c02477
ACS Appl. Nano Mater. 2022, 5, 11423−11428